

Spectrally reconfigurable magnetoplasmonic nanoantenna arrays

Richard M. Rowan-Robinson,^{*,†,||} Jérôme Hurst,^{†,⊥} Agne Ciuciulkaite,[†]
Ioan-Augustin Chioar,[†] Merlin Pohlit,[†] Mario Zapata,[‡] Paolo Vavassori,^{‡,¶}
Alexandre Dmitriev,[§] Peter M. Oppeneer,[†] and Vassilios Kapaklis^{*,†}

[†]*Department of Physics and Astronomy, Uppsala University, Box 516, SE-751 20 Uppsala,
Sweden*

[‡]*CIC nanoGUNE BRTA, E-20018 Donostia-San Sebastian, Spain*

[¶]*IKERBASQUE, Basque Foundation for Science, E-48013 Bilbao, Spain*

[§]*Department of Physics, University of Gothenburg, SE-412 96 Göteborg, Sweden*

^{||}*Present address: Department of Material Science and Engineering, University of Sheffield,
Sheffield, United Kingdom*

[⊥]*Present address: Univ. Grenoble Alpes, CNRS, CEA, Grenoble INP, IRIG-Spintec,
F-38000 Grenoble, France*

E-mail: r.rowan-robinson@sheffield.ac.uk; vassilios.kapaklis@physics.uu.se

Abstract

We have successfully integrated a rare-earth-transition metal (RE-TM) ferrimagnetic alloy, Tb₁₈Co₈₂, with strong out-of-plane magnetic anisotropy, within a gold truncated cone-shaped plasmonic nanoantenna. These hybrid three-dimensional magnetoplasmonic nanoantennas are patterned as extended arrays, resulting in a narrow Fano-type resonance, referred to as a surface lattice mode which arises through the interference of a Rayleigh anomaly and the localized surface plasmon, resulting in abrupt

spectral features for which the Faraday ellipticity is amplified and changes sign in a narrow (≈ 10 nm) spectral window. This magneto-optical surface lattice mode exhibits significant angular dispersion, and we demonstrate and explain using Maxwell-theory simulations, how its spectral position can be tuned by simply varying the angle of incidence. The design concepts presented here can be utilized for the design of a new generation of magnetoplasmonic angle sensors, as well as for the building blocks of magnetoplasmonic nanoantennas suitable for enhancing the light-matter interaction for all-optical switching of the magnetization in RE-TM ferrimagnetic alloys.

Plasmonics as a means to localize and enhance electromagnetic fields, has been successfully applied in the areas of biosensing^{1,2}, optical trapping³, hot-electron transfer⁴, heat-assisted magnetic recording^{5,6}, as well as in the development of integrated photonic circuits^{7,8} and metasurfaces⁹⁻¹². However, for a number of applications, which include modulators and optical switches, but also next-generation plasmonic biosensors^{13,14}, amplification and confinement of the electromagnetic field needs to be accompanied by active tunability. This sub-field, called *active plasmonics*, explores systems where the optical properties can be tuned using an external stimulus¹⁵. Much work has already been devoted to explore mechanisms by which active control of optical responses can be achieved, including, thermal^{14,16,17}, electrical^{18,19}, and chemical approaches^{20,21}. However, there still exists a number of limitations for these active devices, which pertain to combining large tuning bandwidth alongside fast switching times and long-term stability¹⁵.

Magnetoplasmonics merges magnetism with nanophotonics²², where active tunability is achieved through the use of external magnetic fields²³⁻³¹. These fields are used to manipulate the magnetization of the magnetoplasmonic nanoantennas, which in turn affects the optical response, mediated through magneto-optical (M-O) effects. Previously, ferromagnetic plasmonic systems were considered unrealizable, due to the high-optical losses associated with the transition-metal ferromagnets. However, to a large extent, these can be overcome through nanopatterning^{32,33} and materials engineering and fabrication of *hybrid*

noble metal-ferromagnetic nanonantennas³⁴⁻³⁸. Further enhancement is achieved through linewidth engineering^{35,39,40}, where high Q-factor resonances can be engineered in ordered arrays of magnetoplasmonic nanoantennas, exciting surface lattice modes (SLMs). As a direct consequence of the nanoantenna's magnetization, a significant modulation of the plasmonic enhanced M-O effects can be obtained⁴¹. This tunability relates to the magnitude of the Voigt parameter of the ferromagnetic material, as well as to the plasmonic field enhancement of the nanoantenna⁴². Magnetization switching times are sub-ms for magnetic field induced switching²³, reaching ns or even sub-ps timescales if spin-transfer torque⁴³ or all-optical switching mechanisms⁴⁴ are employed. Furthermore, exploiting magnetic anisotropy effects, the magnetization can be stabilised in a desired direction and M-O effects can be recorded at zero external field.

In this letter, we demonstrate the functionalities of a magnetoplasmonic nanoantenna array incorporating an amorphous rare-earth-transition metal (RE-TM) ferrimagnetic alloy, exhibiting perpendicular magnetic anisotropy (PMA)⁴⁵. We show that this hybrid Au/Tb₁₈Co₈₂ system can provide high Q-factor M-O resonances, thus overcoming the losses associated with RE-TM alloys. Using Maxwell-theory modelling, we show that this is achieved through the resonant collective excitation of surface lattice modes (SLMs) which exhibit a strong angular dispersion. This is achieved through the interference of a Rayleigh anomaly with the LSP on the hybrid noble metal RE-TM nanoantenna, giving rise to SLM resonances in both the optical and magneto-optical spectra with characteristic Fano-type asymmetric lineshape. We demonstrate and explain an exceptionally strong spectral tunability of the spectral position of the resonance which can be tuned by varying the angle of incidence of the incoming light, exemplifying the potential of these magnetoplasmonic surfaces for active devices and angular sensors, something which is developing new interest for emerging optical systems⁴⁶.

The use of RE-TM alloys is of particular interest for future magnetoplasmonic devices for three key reasons. First, they are known to exhibit very large M-O activity^{47,48} and there-

fore permit potentially a high M-O tunability. Secondly, they can exhibit strong PMA, yet with an amorphous texture^{45,49–52}. Freire-Fernández et al.⁵³ fabricated magnetoplasmonic Co/Pt nanodots showing PMA, demonstrating tenfold enhancements in M-O activity and the potential of out-of-plane magnetic anisotropy materials in magnetoplasmonic systems. However, the amorphous texture of RE-TM alloys greatly simplifies the otherwise stringent requirements on material microstructure for obtaining these desired magnetic properties. As such, they can be grown on noble metals, such as Au, with minimal residual stresses, and with highly smooth interfaces, thereby maintaining much of their original magnetic properties after lithographic patterning. With PMA, the remanent magnetization state of the Tb₁₈Co₈₂ ferrimagnetic tip can be orientated parallel to the light propagation direction for normal incidence illumination. This allows for direct measurement in the Faraday configuration, without the need of external magnetic fields in order to stabilize the magnetization along the light propagation direction. Thirdly, RE-TM alloys such as Tb₁₈Co₈₂, have experienced renewed interest due to the demonstration of enhanced spin-orbit torques^{54–56} and all-optical switching^{45,57,58}, allowing for zero-field magnetic switching, on picosecond timescales, with the use of pulsed lasers. Demonstrating the compatibility of these materials with plasmonic antennas is of importance for developing sub-diffraction limited all optical switching technologies⁵⁹.

Our nanoantenna structure is based on the plasmonic nanocone geometry which been shown to exhibit a very strong field enhancement⁶⁰ (e.g., effective surface enhanced Raman signal $\sim \times 10^5$), with the electromagnetic field concentrated at the nanocone tip^{60,61}. Large arrays of hybrid Au/Tb₁₈Co₈₂ magnetoplasmonic truncated nanocones (TNCs), as shown schematically in Figure 1a, were fabricated (see Methods, and for material details, see Ciuculkaite et al.⁴⁵). Transmission spectroscopy measurements from two TNC arrays with base diameters, $D_B = 179 \pm 5$ nm and 227 ± 4 nm, are shown in Figure 1d-g. The incidence angle (α_i) was varied, with the sample orientated azimuthally such that momentum component $\vec{k}_{||}$ is directed along either the 340 nm periodicity ($\phi_i = 0$, Figure 1d and f) or the 425 nm

periodicity ($\phi_i = 90^\circ$, Figure 1e and g) directions.

To investigate the potential tunability and reduction in plasmon linewidth achievable through SLMs in hybrid Au/Tb₁₈Co₈₂ nanoantennas, finite-element Maxwell-theory simulations were implemented in COMSOL[®] (see Supporting Information for further details). We simulated truncated nanocones (TNCs), with layer structures of Au(80 nm)/Tb₁₈Co₈₂(15 nm) and base diameter, $D_B = 179$ nm. The choice of dimensions was based on a dimensionality study, where it was observed experimentally that the reduced dimensionality associated with non-truncated nanocones, results in an almost complete loss of any M-O activity (see Supporting Information). The TNCs are arranged in a rectangular array, as schematically shown in the top of Figure 1a, with $a = 340$ nm and $b = 425$ nm periodicity. The incidence angle (using the optical convention), α_i , defines a scattering plane which is either parallel to the xz plane with azimuthal angle $\phi_i = 0$ or parallel to the yx plane with azimuthal angle $\phi_i = 90^\circ$.

SLMs are generally observed close to a Rayleigh anomaly. For a given α_i and lattice periodicity, a Rayleigh anomaly exists where a diffracted order is directed parallel to the grating⁶². This represents the *passing-off* of a diffraction order through a laterally excited beam. There can exist a large number of diffracted modes, which are labeled by two integers n and m . The modes are obtained by imposing that the component of the light wave-vector normal to the lattice surface is real, through the expression

$$k_\perp = \sqrt{k_s^2 - (\mathbf{k}_\parallel + m\mathbf{G}_1 + n\mathbf{G}_2)^2} > 0. \quad (1)$$

In the above formula, $k_s = 2\pi n_{\text{sub}}/\lambda$ corresponds to the light wave-vector in the substrate, where n_{sub} is the refractive index of the fused silica substrate ($n_{\text{sub}} = 1.45$), $\mathbf{k}_\parallel = k_0 [\sin(\alpha_i) \cos(\phi_i) \mathbf{u}_x + \sin(\alpha_i) \sin(\phi_i) \mathbf{u}_y]$ corresponds to the wave-vector component parallel to the lattice surface and $\mathbf{G}_1 = (2\pi/a) \mathbf{u}_x$, $\mathbf{G}_2 = (2\pi/b) \mathbf{u}_y$ are the reciprocal lattice vectors, with \mathbf{u}_x and \mathbf{u}_y being the reciprocal lattice unit vectors. The number of diffraction

modes depends on the lattice dimensions, the angle of incidence, the refractive index of the substrate and the light wavelength. For wavelengths greater than 600 nm, Equation (1) indicates that it is only the diffracted modes ($n = 0 ; m = -1$) for $\phi_i = 0$ and ($n = -1 ; m = 0$) for $\phi_i = 90^\circ$ which can be obtained by varying the incidence angle (see Supporting Information). The analytical expressions for these two substrate modes can be obtained from Equation (1),

$$\lambda_R^{[0,-1]} = a [n_{\text{sub}} + n_{\text{air}} \sin(\alpha_i)] \quad \text{for } \phi_i = 0, \quad (2)$$

$$\lambda_R^{[-1,0]} = b [n_{\text{sub}} + n_{\text{air}} \sin(\alpha_i)] \quad \text{for } \phi_i = 90^\circ, \quad (3)$$

where n_{air} is the refractive index of air.

The calculated transmission spectra are shown in Figures 1b and c, and in all the calculations (and subsequent measurements) the light is p -polarised, such that the incident electric field lies in the scattering plane. It can be seen that an LSP is excited at 690 nm when the array is illuminated at normal incidence ($\alpha_i = 0^\circ$). This LSP is associated with an electric dipole-type plasmon, which for $\phi_i = 0^\circ$ (Figure 1b) oscillates in the xz scattering plane and for $\phi_i = 90^\circ$ (Figure 1c) oscillates in the yz scattering plane. In Figure 1b, for which $\phi_i = 0$; $\lambda_R^{[0,-1]}$ is associated with modes along the 340 nm periodicity and is tunable through α_i . Analysing the allowed $\lambda_R^{[n,m]}$ from Eq. (2), we find that for $a = 340$ nm, $\lambda_R^{[0,-1]} = 493$ nm, 552 nm, 581 nm and 609 nm for $\alpha_i = 0, 10, 15$, and 20 degrees, respectively. Since for $\phi_i = 0$ the scattering plane is orthogonal to the 425 nm periodicity, for all α_i , $\lambda_R^{[-1,0]} = 616$ nm. As such, there is no spectral overlap of any $\lambda_R^{[n,m]}$ with the localized surface plasmon (LSP) and the transmission spectra show no dependence on α_i for the range of α_i investigated.

When $\phi_i = 90^\circ$ (Figure 1c), α_i operates within the yz scattering plane and we use Eq. (3) to calculate $\lambda_R^{[-1,0]}$. Here, $\lambda_R^{[-1,0]}$ can be tuned with α_i , and $\lambda_R^{[0,-1]} = 493$ nm for all α_i due to the orthogonality between the new scattering plane and the 340 nm periodicity. In this configuration, substantial tuning of the transmission spectrum is possible through the

variation of α_i . The high sensitivity of the spectra to α_i is a result of the strong overlap of $\lambda_R^{[-1,0]}$ with the LSP, whereby $\lambda_R^{[-1,0]} = 616$ nm, 690 nm, 726 nm and 762 nm for $\alpha_i = 0, 10, 15$, and 20 degrees, respectively, which is in excellent agreement with the abrupt spectral features observed in Figure 1c, as indicated by the coloured arrows.

In the Fano-type resonance description^{63,64}, the LSP mode represents a continuum of states, whereas the Rayleigh anomaly represents a narrow mode, which upon interfering with the continuum, results in the characteristic asymmetric lineshape of the SLM. A similar behaviour in magnetoplasmonic nanoantennas has been demonstrated for pure Ni nanoantennas, by Maccaferri et al.⁴⁰ and Kataja et al.³⁹. In these studies, the overlap between $\lambda_R^{[n,m]}$ and the LSP was tuned by varying the lattice periodicity of the magnetoplasmonic crystal. Here, we show that there is a much simpler alternative, whereby the SLM can be tuned by exploiting the angular dispersion of $\lambda_R^{[n,m]}$, in effect allowing dynamic lineshape engineering in a single sample. Such behaviour has been observed in the transmission/reflectance of non-magnetic plasmonic arrays⁶⁵, but this is the first demonstration of angular tunability in a magnetoplasmonic system, for which M-O effects can be explored.

The dipolar radiation field is strongest transverse to the dipolar LSP oscillation axis given by p_E . In our simulations we used p -polarised light and hence the electric dipole excitation within individual TNCs is orientated within the scattering plane and parallel to the diffraction anomaly. However, since this dipole can not radiate along the oscillation direction, there must exist an additional mechanism for light to be scattered along the 425 nm periodicity direction for the excitation of the Rayleigh anomaly and resulting SLM observed in Figure 1c. With illumination at oblique incidence, there is the possibility to excite an out-of-plane component to the electric dipole, which we further confirmed by COMSOL® simulations in the Supporting Information. This out-of-plane dipolar component would radiate in all directions within the plane of the lattice⁶⁶, and hence is responsible for the excitation of all $\lambda_R^{[n,m]}$, e.g. $[-1, 0]$, $[0, -1]$, $[-1, -1]$ modes for p -polarised light.

The measured transmission spectra are shown in Figure 1d-g, for which in the $\phi_i = 0$

configuration, for the α_i investigated, $\lambda_R^{[0,-1]}$ does not overlap with the LSP and the transmission spectra show little dependence on α_i . This is in agreement with COMSOL[®] simulations for $D_B = 179$ nm, although the LSP itself exhibits a red-shift alongside some spectral broadening, which could be a result of the Al_2O_3 layer and oxidation of the exposed $\text{Tb}_{18}\text{Co}_{82}$ side-walls on the fabricated TNCs. In Figures 1d and f, there is a feature between 500 - 600 nm which migrates to longer wavelengths as α_i increases which is most likely due to $\lambda_R^{[0,-1]}$, since it occurs at the same spectral positions for both the $D_B = 179$ nm and 227 nm samples, suggesting its origin relates to the lattice and not the LSP resonance.

When the sample is rotated into the $\phi_i = 90^\circ$ configuration (Figures 1f and g), strong variations in the transmission spectra are observed. These are in good agreement with the COMSOL[®] simulations, in both spectral position and lineshape, albeit with reduced amplitude. For both $D_B = 227$ and 179 nm samples, the $\alpha_i = 0$ measurements show a small blue shift of the LSP for the $\phi_i = 90^\circ$ configuration relative to the $\phi_i = 0$ configuration. As shown in the inset scanning electron microscopy images, the TNCs are not perfectly circular and this discrepancy is likely a result of this. The transmission spectra between the two samples differ, even though they have identical periodicities. These differences are driven by the different LSP resonances, where the larger $D_B = 227$ nm TNCs exhibit a broader linewidth than the smaller $D_B = 179$ nm TNC array. The broad spectral distribution of the $D_B = 227$ nm TNC allows for a larger tuning bandwidth, such that there exists a larger range of α_i for which $\lambda_R^{[-1,0]}$ overlaps with the LSP. In fact, in this case the high plasmonic losses associated with the $\text{Tb}_{18}\text{Co}_{82}$ layer increase the available bandwidth for tuning and demonstrates an important trade-off that should be considered in future angular sensor device designs.

The Fano-like resonances in the transmission spectra, although tunable, are still relatively broad. However, resonances in M-O spectra can yield higher Q-factors⁶⁷ and we now discuss the M-O activity of these samples. Maccaferri et al.⁶⁸ showed that an out-of-plane magnetization in the presence of the electric dipolar plasmon gives rise to a magneto-optical dipolar

plasmon (p_{MO}) which is orientated orthogonal to p_{E} and is induced in the ferromagnetic layer. This transverse oscillation is induced via spin-orbit coupling, generating an oscillation of conduction electrons in-the-plane but orthogonal to p_{E} . With the use of p -polarised light, the pure optical dipole is orientated along p_{E} and the transverse M-O dipole is aligned along p_{MO} , as shown in the accompanying schematics on the far-left of Figure 2. Hence, the use of p -polarised light results in the M-O dipole induced in the $\text{Tb}_{18}\text{Co}_{82}$ layer which radiates strongly in the scattering plane, and is therefore expected to be most sensitive to the angular dispersion of the SLM as the magnetoplasmonic lattice is rotated through α_i .

In Figure 2 the Faraday rotation (θ_{F}), Faraday ellipticity (η_{F}) and Faraday angle ($\Theta_{\text{F}} = \sqrt{\theta_{\text{F}}^2 + \eta_{\text{F}}^2}$) are presented. COMSOL[®] simulations of the Faraday effect using permittivity values measured for a $\text{Tb}_{18}\text{Co}_{82}$ thin film are shown in Figure 2 (left column) for the $D_{\text{B}} = 179$ nm TCN array (see Supporting Information for details). Through fitting a Lorentzian to the $\alpha_i = 0$ transmission and Θ_{F} spectra for the $\phi_i = 0$ configuration shown in Figures 1b and 2a, it is estimated from the COMSOL[®] simulations that the M-O resonance exhibits a two-fold reduction in linewidth relative to the pure optical resonance. As with the transmission curves, Θ_{F} shows no angular dependence for this configuration where the $\lambda_{\text{R}}^{[0,-1]}$ mode is activated, which does not exhibit spectral overlap with the LSP. This behaviour is reproduced in the measured $D_{\text{B}} = 179$ nm and $D_{\text{B}} = 227$ nm arrays in Figures 2b and c respectively.

Alike the transmission spectra, the Faraday spectra show strong dependence in the $\phi_i = 90^\circ$ configuration and suggest that sizeable Faraday angles of up to 0.3° can be obtained. The simulated spectra (left column) suggest that extremely sharp features exist, coinciding with $\lambda_{\text{R}}^{[-1,0]}$, as indicated by the coloured arrows. The Rayleigh anomaly is strongest through the substrate and the observation of strong diffractive effects in the Faraday spectra indicates that the M-O dipole induced in the $\text{Tb}_{18}\text{Co}_{82}$ layer is transferred to the rest of the TNC through proximity, in agreement with Pourjamal et al.³⁷.

The experimental M-O spectra measured for the $D_{\text{B}} = 179$ nm TNCs, shown in Figure 2 (middle column, e, h, and k), the curves compare very well to those obtained from the

calculations for the same structure shown in Figure 2 (left column, d, g and j), again, albeit with a slightly reduced amplitude. The excellent reproduction of the measured spectra through COMSOL[®] simulations demonstrates the suitability of combining finite-element methods with experimentally measured *thin-film* permittivity values for the design of magnetoplasmonic devices. For the $D_B = 227$ nm TNCs, as shown in Figure 2 (right column, f, i and l), there is a stronger Faraday effect, but with broader spectral features, demonstrating the trade-off between incorporating more magnetic material in the nanoantenna whilst maintaining small dimensions for narrow plasmonic resonances.

It is clear that *off-resonance* it is not possible to measure the magneto-optical response from the $\text{Tb}_{18}\text{Co}_{82}$ nanocones, where values of θ_F and η_F quickly reduce to values comparable to the measurement uncertainty. In effect, the LSP amplifies the minute magnetic signals which ordinarily wouldn't be resolvable with a conventional M-O measurement. From scanning electron microscopy images taken post ion beam milling, it is possible to estimate the truncation diameter (D_T). For the $D_B = 179$ nm TNC arrays, this amounts to a $\text{Tb}_{18}\text{Co}_{82}$ disk with $D_T = 86 \pm 10$ nm. This yields a percentage $\text{Tb}_{18}\text{Co}_{82}$ coverage (ρ_c) of 4%, which can be considered as an effective thickness of $\rho_c t_{\text{TbCo}}$, where $t_{\text{TbCo}} = 15$ nm is the $\text{Tb}_{18}\text{Co}_{82}$ thickness within the TNC. Astonishingly, this yields an effective thickness (i.e. the thickness of a film made with the same quantity of material) of approximately 0.6 nm, of the order of one monolayer, demonstrating the enormous amplification obtained through the LSP.

The experimental θ_F , η_F and Θ_F curves all show abrupt features that onset with the excitation of the SLM associated with $\lambda_R^{[-1,0]}$ in the $\phi_i = 90^\circ$ configuration. Just prior to the SLM, there is the greatest change in M-O activity for the smallest change in wavelength. Since this feature is dependent on the spectral position of $\lambda_R^{[-1,0]}$, it can be tuned by varying α_i , indicating the potential use of such devices as angular sensors. This is explored in Figure 3a, where hysteresis loops are recorded through measurements of the transmitted light ellipticity at a wavelength of 730 nm for the $D_B = 227$ nm TNC array for different α_i . The $\text{Tb}_{18}\text{Co}_{82}$ tips maintain PMA even after the lithography process, which is clear from

the large remanent magnetization observed in the hysteresis loops in Figure 3a, reducing the magnetic field strength required to saturate the sample along the out-of-plane direction.

The dynamic tuning of the M-O activity available through varying α_i is profound, resulting in a dramatic change in the magnitude of η_F , where extraordinarily at $\alpha_i = 15^\circ$ the loop is inverted. The inset in Figure 3a shows a magnified view of η_F for the spectral region around the SLM; it is clear that this sign change in η_F is associated with the migration of the SLM to the measurement wavelength of 730 nm. This is explored further in Figure 3b where the change in Faraday ellipticity ($\delta\eta_F$) between successive wavelength increments ($\Delta\lambda = 5$ nm) is plotted. Since the gradient of this spectral feature is positive, the $\delta\eta_F < 0$ data has been excluded from the fits.

It is evident that $\delta\eta_F$ is largest in this region where η_F undergoes a sign change, which in turn is tunable by varying α_i . This dynamic tuning of the SLM could be used in refractive index sensing where the spectral region of maximum sensitivity can be tuned by varying the angle of incidence, thereby allowing the user to operate in a spectral region where the solute (e.g. blood, water) is minimally absorbing⁶⁹. Alternatively, deviations from a set angle or tilt could be measured in terms of reduced magneto-optical activity for applications in control systems.

Lorentzian functions have been fitted to the $\delta\eta_F$ data, in order to estimate the spectral width of this abrupt transition in η_F . Due to the limited number of data points on this abrupt spectral transition, a reliable estimate of the FWHM is difficult to obtain from these fits, however, all values are within the 5-10 nm range (which is comparable to the wavelength resolution of the setup) with the exception of the $\alpha_i = 10^\circ$ where a FWHM of 24 ± 10 nm is obtained due to the anomalously large error on this particular measurement.

The PMA in these samples allows for the measurement of the magnetic differential absorption of circularly polarised light (which underpins η_F), without the need for a large out-of-plane magnetic field to stabilize the magnetization along the propagation direction of the light. A time varying polarisation light helicity is incident on the sample and we

measure the ratio, $C_{\omega}^q/C_{\omega}^q$ which is proportional to the differential absorption of circularly polarised light (see Methods) for the two opposing polar magnetization states ($q = \pm M$). Figure 4a shows several spectra for the $D_B = 227$ nm sample for different values of α_i , in the $\phi_i = 90^\circ$ configuration and zero magnetic field. The spectra minima strongly depend on α_i . Furthermore, the amplitude of $C_{\omega}^q/C_{\omega}^q$ can be modulated by reversing the magnetization ($q = +M_z \rightarrow -M_z$, and *vice versa*), as indicated by the variation between the dashed and solid curves. The TNC array therefore exhibits active tunability, whereby absolute transmission can be enhanced or attenuated with the use of a magnetic field. Similar effects have been observed by Zubritskaya et al.³⁴ for a magnetoplasmonic trimer system, however, a field was required to orient the magnetization out-of-plane throughout the measurement, whereas in this study a field is only required to initialise the magnetic state. An additional tuning is incorporated through α_i whereby the spectral location of this maximum for magnetic modulation can be tuned with the SLM. Additionally, by using a class of material known to exhibit all-optical switching⁴⁵, this could enable the removal of the external field entirely, whereby the transmission would be modulated remotely using a laser^{57,59}, avoiding the need for electromagnet coils which are challenging to miniaturise.

The difference between the measured helicity dependent transmission between the two antiparallel magnetization states gives the available magnetic modulation (see Methods) which is plotted in Figure 4c. The dispersion of the SLM calculated from equation (3) is given by the dashed lines. Here, it is clear that the SLM dictates the onset wavelength for the magnetic modulation of the differential circular transmission, meaning that the peak sensitivity can be tuned to any wavelength between 650 nm - 800 nm. This tunability range is governed by the FWHM of the LSP in the transmission spectra. Modest modulations of around 0.5% are obtained, however, we believe there is enormous scope for improvement through optimisation of RE-TM and Au thicknesses alongside the nanoantenna geometry, including exploring new geometries which can exhibit plasmonic *dark-modes*, which result in a stronger plasmonic enhancement of the M-O activity than can be achieved with the

dipolar plasmons in this study⁷⁰.

In conclusion, we demonstrated the successful integration of a RE-TM materials within a hybrid magneto-plasmonic nanoantenna array. A strong angular dispersion is obtained through the interference of the Rayleigh anomaly and the LSP, producing a sharp SLM in both the optical and M-O spectra. We showcase dynamic tunability of the SLM using the light incidence angle, which modifies the M-O response of the sample, as we explained using Maxwell-theory simulations. In addition, we measured the magnetic modulation of the differential circular transmission of the samples in a zero field measurement, exploiting the PMA present in the TNCs. Similar tunability was observed in these measurements as that obtained in the Faraday effect measurements, but with the underlying phenomena being related to the magnetic circular dichroism of the $\text{Tb}_{18}\text{Co}_{82}$ layer. The integration of RE-TM materials within plasmonic systems, as shown here in our work, offers great promise for highly tunable, fast all-optical switching, active plasmonic devices^{22,59}.

Methods

Sample Fabrication

The plasmonic nanoantennas are fabricated using a top-down approach, based on the method outlined by Horrer et al.⁶⁰. Au(80 nm) films were deposited using electron-beam evaporation onto glass substrates. Later, Al_2O_3 (3.5 nm)/ $\text{Tb}_{18}\text{Co}_{82}$ (15 nm)/ Al_2O_3 (2 nm) films were sputter deposited onto these films, with the complete structure being Au(80 nm)/ Al_2O_3 (3.5 nm)/ $\text{Tb}_{18}\text{Co}_{82}$ (15 nm)/ Al_2O_3 (2 nm). The $\text{Tb}_{18}\text{Co}_{82}$ layer was deposited through co-sputtering. The additional thin Al_2O_3 layers were used as capping and isolating layers for the $\text{Tb}_{18}\text{Co}_{82}$. Here, the composition of the film can be varied by adjusted the relative power of the Co and Tb magnetrons. Calibration films were made with different power ratios on the two magnetrons and compositions were verified using Rutherford back scattering. Electron beam lithography was used to define disk shaped apertures in a MicroChem 496PMMA A4 electron-beam resist. Electron-beam evaporation was used to deposit an Al mask through the resist

followed by removal of the PMMA mask with Acetone. The resulting structure was then milled at a 5 deg incidence angle with sample rotation, removing all material unprotected by the Al mask. Any remaining Al mask was then removed with the photoresist developer microdeposit 351, which in this case was used as a selective etcher to target the Al. A conical profile is induced through a combination of the small lateral component of the milling which depends to some extent on the small milling incidence angle⁷¹. In our samples, this results in a constant slope profile of approximately 62 deg for all nanoantenna arrays. Therefore, by varying the diameter of the Al mask, the resulting structures can be tuned from truncated to conical profiles.

Magneto-optical characterisation

The experimental values of θ_F , η_F and Θ_F were measured using the photoelastic modulator methodology with an applied field of 450 mT along the light propagation direction, which is described in the Supporting Information. A quadratic polynomial was fitted to the raw θ_F data in order to subtract the background contribution which arises from the Faraday rotation of the fused-silica substrate, which is strongest for short wavelengths and decreases for longer wavelengths⁷².

For the differential absorption of circularly polarised light measurement, a time varying light polarisation, which alternates between left and right circularly polarised light states at 50 kHz was generated using a photoelastic modulator (PEM) and directed at the sample at normal incidence. This is achieved by passing linearly polarised light orientated at 45° to the fast axis of the PEM, with the PEM retardation set to 0.25 wavelengths. Any mechanism in the TNC array which results in a difference in absorption for opposite helicities (including magnetic circular dichroism) will contribute to an oscillating light intensity at the detector at the photoelastic modulator frequency. It is common to express this measurement as the ratio C_ω^q/C_o^q , where C_ω^q is the amplitude of the $\omega = 50$ kHz signal for a fixed polar magnetization $q = \pm M_z$, and C_o^q is the DC signal intensity, which contains the helicity

independent absorption contribution. Prior to the measurement, a saturating magnetic field was used to initialise the magnetization along the light propagation direction ($q = +M_z$) and then removed. For the subsequent measurement, the magnetization was saturated in the opposite polar direction ($q = -M_z$) and the measurement repeated.

It is important to note that the spectra in Figure 4a contains additional *fake* CD contributions, which arise from leaking-in of the large linear dichroism signal as a result of the rectangular array with which the nanostructures are arranged. By observing the difference between the antiparallel magnetization states, namely $\Delta[C_\omega/C_o]$, these effects, which are independent of the magnetization, can be subtracted out, yielding the available magnetic modulation. We define this magnetic modulation of the helicity dependent transmission as $(C_\omega^{-M_z} - C_\omega^{+M_z})/(C_o^{-M_z} + C_o^{+M_z})$, and this quantity is plotted in Figure 4c as a function of both α_i and wavelength.

Acknowledgement

The authors would like to express their gratitude towards Prof. Bengt Lindgren of Uppsala University, Sweden, for fruitful discussions and support with the ellipsometric characterization of TbCo thin film materials. The excellent support and infrastructure of the MyFab facility at the Ångström Laboratory of Uppsala University is also highly appreciated. The authors acknowledge support from the Knut and Alice Wallenberg Foundation project “*Harnessing light and spins through plasmons at the nanoscale*” (Project No. 2015.0060), the Swedish Research Council (Project No. 2019-03581), the Swedish Foundation for International Cooperation in Research and Higher Education (Project No. KO2016-6889), and the Swedish National Infrastructure for Computing (SNIC). This work is part of a project which has received funding from the European Union’s Horizon 2020 research and innovation programme under grant agreement no. 737093, “*FEMTOTERABYTE*”.

References

- (1) Mejía-Salazar, J. R.; Oliveira, O. N. *Chemical Reviews* **2018**, *118*, 10617–10625.
- (2) Biacore Handbook. <https://www.biacore.com/lifesciences/service/downloads/Handbooks/>, General Electric Healthcare.
- (3) Crozier, K. B. *Light: Science & Applications* **2019**, *8*, 35.
- (4) Shan, H. et al. *Light: Science & Applications* **2019**, *8*, 9.
- (5) Challener, W. A.; Peng, C.; Itagi, A. V.; Karns, D.; Peng, W.; Peng, Y.; Yang, X.; Zhu, X.; Gokemeijer, N. J.; Hsia, Y.-T.; Ju, G.; Rottmayer, R. E.; Seigler, M. A.; Gage, E. C. *Nature Photonics* **2009**, *3*, 220–224.
- (6) Gosciniaik, J.; Mooney, M.; Gubbins, M.; Corbett, B. *Scientific Reports* **2016**, *6*, 24423.
- (7) Sorger, V. J.; Oulton, R. F.; Ma, R.-M.; Zhang, X. **2012**, 11.
- (8) Ozbay, E. *Science* **2006**, *311*, 189–193.
- (9) Spektor, G.; David, A.; Gjonaj, B.; Bartal, G.; Orenstein, M. *Nano Letters* **2015**, *15*, 5739–5743.
- (10) Pendry, J. B.; Schurig, D.; Smith, D. R. *Science* **2006**, *312*, 1780–1782.
- (11) Schurig, D.; Mock, J. J.; Justice, B. J.; Cummer, S. A.; Pendry, J. B.; Starr, A. F.; Smith, D. R. *Science* **2006**, *314*, 977–980.
- (12) Yu, N.; Capasso, F. *Nature Materials* **2014**, *13*, 139–150.
- (13) Zhu, A. Y.; Yi, F.; Reed, J. C.; Zhu, H.; Cubukcu, E. *Nano Letters* **2014**, *14*, 5641–5649.
- (14) Toma, M.; Jonas, U.; Mateescu, A.; Knoll, W.; Dostalek, J. *The Journal of Physical Chemistry C* **2013**, *117*, 11705–11712.

- (15) Jiang, N.; Zhuo, X.; Wang, J. *Chemical Reviews* **2018**, *118*, 3054–3099.
- (16) Suh, J. Y.; Donev, E. U.; Lopez, R.; Feldman, L. C.; Haglund, R. F. *Applied Physics Letters* **2006**, *88*, 133115.
- (17) Rudé, M.; Simpson, R. E.; Quidant, R.; Pruneri, V.; Renger, J. *ACS Photonics* **2015**, *2*, 669–674.
- (18) Dabidian, N.; Kholmanov, I.; Khanikaev, A. B.; Tatar, K.; Trendafilov, S.; Mousavi, S. H.; Magnuson, C.; Ruoff, R. S.; Shvets, G. *ACS Photonics* **2015**, *2*, 216–227.
- (19) Novo, C.; Funston, A. M.; Gooding, A. K.; Mulvaney, P. *Journal of the American Chemical Society* **2009**, *131*, 14664–14666.
- (20) Sun, Z.; Ni, W.; Yang, Z.; Kou, X.; Li, L.; Wang, J. *Small* **2008**, *4*, 1287–1292.
- (21) Jiang, N.; Shao, L.; Wang, J. *Advanced Materials* **2014**, *26*, 3282–3289.
- (22) Maccaferri, N.; Zubritskaya, I.; Razdolski, I.; Chioar, I.-A.; Belotelov, V.; Kapaklis, V.; Oppeneer, P. M.; Dmitriev, A. *Journal of Applied Physics* **2020**, *127*, 080903.
- (23) Temnov, V. V.; Armelles, G.; Woggon, U.; Guzatov, D.; Cebollada, A.; Garcia-Martin, A.; Garcia-Martin, J.-M.; Thomay, T.; Leitenstorfer, A.; Bratschitsch, R. *Nature Photonics* **2010**, *4*, 107–111.
- (24) Zhang, M. et al. *Nature Nanotechnology* **2017**, *12*, 228–232.
- (25) Torrado, J. F.; González-Díaz, J. B.; González, M. U.; García-Martín, A.; Armelles, G. *Optics Express* **2010**, *18*, 15635–15642.
- (26) Belotelov, V. I.; Doskolovich, L. L.; Zvezdin, A. K. *Physical Review Letters* **2007**, *98*, 077401.

- (27) Belotelov, V. I.; Akimov, I. A.; Pohl, M.; Kotov, V. A.; Kasture, S.; Vengurlekar, A. S.; Venu, G. A.; Yakovlev, D. R.; Zvezdin, A. K.; Bayer, M. *Nature Nanotech.* **2011**, *4*, 1–7.
- (28) González-Díaz, J. B.; García-Martín, A.; Armelles, G.; García-Martín, J. M.; Clavero, C.; Cebollada, A.; Lukaszew, R. A.; Skuza, J. R.; Kumah, D. P.; Clarke, R. *Phys. Rev. B* **2007**, *76*, 153402.
- (29) Rowan-Robinson, R. M.; Melander, E.; Chioar, I.-A.; Caballero, B.; García-Martín, A.; Papaioannou, E. T.; Kapaklis, V. *AIP Advances* **2019**, *9*, 025317.
- (30) Rollinger, M.; Thielen, P.; Melander, E.; Östman, E.; Kapaklis, V.; Obry, B.; Cinchetti, M.; García-Martín, A.; Aeschlimann, M.; Papaioannou, E. T. *Nano Letters* **2016**, *16*, 2432–2438.
- (31) Lodewijks, K.; Maccaferri, N.; Pakizeh, T.; Dumas, R. K.; Zubritskaya, I.; Åkerman, J.; Vavassori, P.; Dmitriev, A. *Nano Letters* **2014**, *14*, 7207–7214.
- (32) Ctistis, G.; Papaioannou, E.; Patoka, P.; Gutek, J.; Fumagalli, P.; Giersig, M. *Nano Letters* **2009**, *9*, 1–6.
- (33) Papaioannou, E. T.; Kapaklis, V.; Giersig, M.; Fumagalli, P.; García-Martín, A.; Ferreiro-Vila, E.; Ctistis, G. *Physical Review B* **2010**, *81*, 054424.
- (34) Zubritskaya, I.; Maccaferri, N.; Inchausti Ezeiza, X.; Vavassori, P.; Dmitriev, A. *Nano Letters* **2018**, *18*, 302–307.
- (35) Kataja, M.; Pourjamal, S.; Maccaferri, N.; Vavassori, P.; Hakala, T. K.; Huttunen, M. J.; Törmä, P.; van Dijken, S. *Optics Express* **2016**, *24*, 3652–3662.
- (36) Martin-Becerra, D.; Gonzalez-Diaz, J. B.; Temnov, V. V.; Cebollada, A.; Armelles, G.; Thomay, T.; Leitenstorfer, A.; Bratschitsch, R.; Garcia-Martin, A.; Gonzalez, M. U. *Applied Physics Letters* **2010**, *97*, 183114.

- (37) Pourjamal, S.; Kataja, M.; Maccaferri, N.; Vavassori, P.; van Dijken, S. *Nanophotonics* **2018**, *7*, 905–912.
- (38) Bant  , J. C.; Meneses-Rodr  guez, D.; Garc  a, F.; Gonz  lez, M. U.; Garc  a-Mart  n, A.; Cebollada, A.; Armelles, G. *Advanced Materials* **2012**, *24*, OP36–OP41.
- (39) Kataja, M.; Hakala, T. K.; Julku, A.; Huttunen, M. J.; van Dijken, S.; T  rm  , P. *Nature Communications* **2015**, *6*, ncomms8072.
- (40) Maccaferri, N.; Bergamini, L.; Pancaldi, M.; Schmidt, M. K.; Kataja, M.; van Dijken, S.; Zabala, N.; Aizpurua, J.; Vavassori, P. *Nano Letters* **2016**, *16*, 2533–2542.
- (41) Moncada-Villa, E.; Garc  a-Mart  n, A.; Cuevas, J. C. *Physical Review B* **2014**, *90*, 085120.
- (42) Gonz  lez-D  az, J. B.; Garc  a-Mart  n, A.; Garc  a-Mart  n, J. M.; Cebollada, A.; Armelles, G.; Sep  lveda, B.; Alaverdyan, Y.; K  ll, M. *Small* **2008**, *4*, 202–205.
- (43) Garelo, K.; Avci, C. O.; Miron, I. M.; Baumgartner, M.; Ghosh, A.; Auffret, S.; Boulle, O.; Gaudin, G.; Gambardella, P. *Applied Physics Letters* **2014**, *105*, 212402.
- (44) Vahaplar, K.; Kalashnikova, A. M.; Kimel, A. V.; Hinzke, D.; Nowak, U.; Chantrell, R.; Tsukamoto, A.; Itoh, A.; Kirilyuk, A.; Rasing, T. *Physical Review Letters* **2009**, *103*, 117201.
- (45) Ciuciulkaite, A.; Mitra, K.; Moro, M. V.; Chioar, I.-A.; Rowan-Robinson, R. M.; Parchenko, S.; Kleibert, A.; Lindgren, B.; Andersson, G.; Davies, C.; Kimel, A.; Kirilyuk, A.; Kapaklis, V. *arXiv* **2020**, 2002.07544.
- (46) Haghtalab, M.; Tamagnone, M.; Zhu, A. Y.; Safavi-Naeini, S.; Capasso, F. *ACS Photonics* **2020**, *7*, 991–1000.
- (47) Buschow, K. H. J. *Journal of the Less Common Metals* **1989**, *155*, 307–318.

- (48) Atkinson, R.; Gamble, R.; Gu, P. F.; Lissberger, P. H. *Thin Solid Films* **1988**, *162*, 89–100.
- (49) Yoshino, S.; Takagi, H.; Tsunashima, S.; Masuda, M.; Uchiyama, S. *Japanese Journal of Applied Physics* **1984**, *23*, 188.
- (50) Hebler, B.; Hassdenteufel, A.; Reinhardt, P.; Karl, H.; Albrecht, M. *Frontiers in Materials* **2016**, *3*.
- (51) Harris, V. G.; Aylesworth, K. D.; Das, B. N.; Elam, W. T.; Koon, N. C. *Physical Review Letters* **1992**, *69*, 1939–1942.
- (52) Frisk, A.; Magnus, F.; George, S.; Arnalds, U. B.; Andersson, G. *Journal of Physics D: Applied Physics* **2016**, *49*, 035005.
- (53) Freire-Fernández, F.; Mansell, R.; van Dijken, S. *Physical Review B* **2020**, *101*, 054416.
- (54) Finley, J.; Liu, L. *Physical Review Applied* **2016**, *6*.
- (55) Ueda, K.; Mann, M.; Pai, C.-F.; Tan, A.-J.; Beach, G. S. D. *Applied Physics Letters* **2016**, *109*, 232403.
- (56) Ueda, K.; Mann, M.; de Brouwer, P. W. P.; Bono, D.; Beach, G. S. D. *Physical Review B* **2017**, *96*.
- (57) Alebrand, S.; Gottwald, M.; Hehn, M.; Steil, D.; Cinchetti, M.; Lacour, D.; Fullerton, E. E.; Aeschlimann, M.; Mangin, S. *Applied Physics Letters* **2012**, *101*, 162408.
- (58) Mangin, S.; Gottwald, M.; Lambert, C.-H.; Steil, D.; Uhlíř, V.; Pang, L.; Hehn, M.; Alebrand, S.; Cinchetti, M.; Malinowski, G.; Fainman, Y.; Aeschlimann, M.; Fullerton, E. E. *Nature Materials* **2014**, *13*, 286–292.
- (59) Liu, T.-M. et al. *Nano Lett.* **2015**, *15*, 6862–6868.

- (60) Horrer, A.; Schäfer, C.; Broch, K.; Gollmer, D. A.; Rogalski, J.; Fulmes, J.; Zhang, D.; Meixner, A. J.; Schreiber, F.; Kern, D. P.; Fleischer, M. *Small* **2013**, *9*, 3987–3992.
- (61) Schäfer, C.; A. Gollmer, D.; Horrer, A.; Fulmes, J.; Weber-Bargioni, A.; Cabrini, S.; James Schuck, P.; P. Kern, D.; Fleischer, M. *Nanoscale* **2013**, *5*, 7861–7866.
- (62) Rayleigh, L. *Proceedings of the Royal Society of London Series A* **1907**, *79*, 399–416.
- (63) Fano, U. *Phys. Rev.* **1961**, *124*, 1866–1878.
- (64) Luk'yanchuk, B.; Zheludev, N. I.; Maier, S. A.; Halas, N. J.; Nordlander, P.; Giessen, H.; Chong, C. T. *Nature Materials* **2010**, *9*, 707–715.
- (65) Vecchi, G.; Giannini, V.; Gómez Rivas, J. *Physical Review B* **2009**, *80*, 201401.
- (66) Huttunen, M. J.; Dolgaleva, K.; Törmä, P.; Boyd, R. W. *Optics Express* **2016**, *24*, 28279.
- (67) Qin, J.; Zhang, Y.; Liang, X.; Liu, C.; Wang, C.; Kang, T.; Lu, H.; Zhang, L.; Zhou, P.; Wang, X.; Peng, B.; Hu, J.; Deng, L.; Bi, L. *ACS Photonics* **2017**, *4*, 1403–1412.
- (68) Maccaferri, N.; Berger, A.; Bonetti, S.; Bonanni, V.; Kataja, M.; Qin, Q. H.; van Dijken, S.; Pirzadeh, Z.; Dmitriev, A.; Nogués, J.; Åkerman, J.; Vavassori, P. *Physical Review Letters* **2013**, *111*, 167401.
- (69) Kazuma, E.; Tatsuma, T. *Nanoscale* **2013**, *6*, 2397–2405.
- (70) López-Ortega, A.; Herrera, M. Z.; Maccaferri, N.; Pancaldi, M.; Garcia, M.; Chuvilin, A.; Vavassori, P. *Light: Science & Applications* **2020**, *9*, 49.
- (71) Fleischer, M.; Zhang, D.; Braun, K.; Jäger, S.; Ehlich, R.; Häffner, M.; Stanciu, C.; Hörber, J. K. H.; Meixner, A. J.; Kern, D. P. *Nanotechnology* **2010**, *21*, 065301.
- (72) Qiu, J.; Hirao, K. *Journal of Materials Research* **1998**, *13*, 1358–1362.

Supporting Information:

Spectrally reconfigurable magnetoplasmonic nanoantenna arrays

Richard M. Rowan-Robinson,^{*,†,||} Jérôme Hurst,^{†,⊥} Agne Ciuciulkaite,[†]
Ioan-Augustin Chioar,[†] Merlin Pohlitz,[†] Mario Zapata,[‡] Paolo Vavassori,^{‡,¶}
Alexandre Dmitriev,[§] Peter M. Oppeneer,[†] and Vassilios Kapaklis^{*,†}

[†]*Department of Physics and Astronomy, Uppsala University, Box 516, SE-751 20 Uppsala, Sweden*

[‡]*CIC nanoGUNE, E-20018 Donostia-San Sebastian, Spain*

[¶]*IKERBASQUE, Basque Foundation for Science, E-48013 Bilbao, Spain*

[§]*Department of Physics, University of Gothenburg, SE-412 96 Göteborg, Sweden*

^{||}*Present address: Department of Material Science and Engineering, University of Sheffield, Sheffield, United Kingdom*

[⊥]*Present address: Univ. Grenoble Alpes, CNRS, CEA, Grenoble INP, IRIG-Spintec, F-38000 Grenoble, France*

E-mail: r.rowan-robinson@sheffield.ac.uk; vassilios.kapaklis@physics.uu.se

Spectral Faraday polarimetry

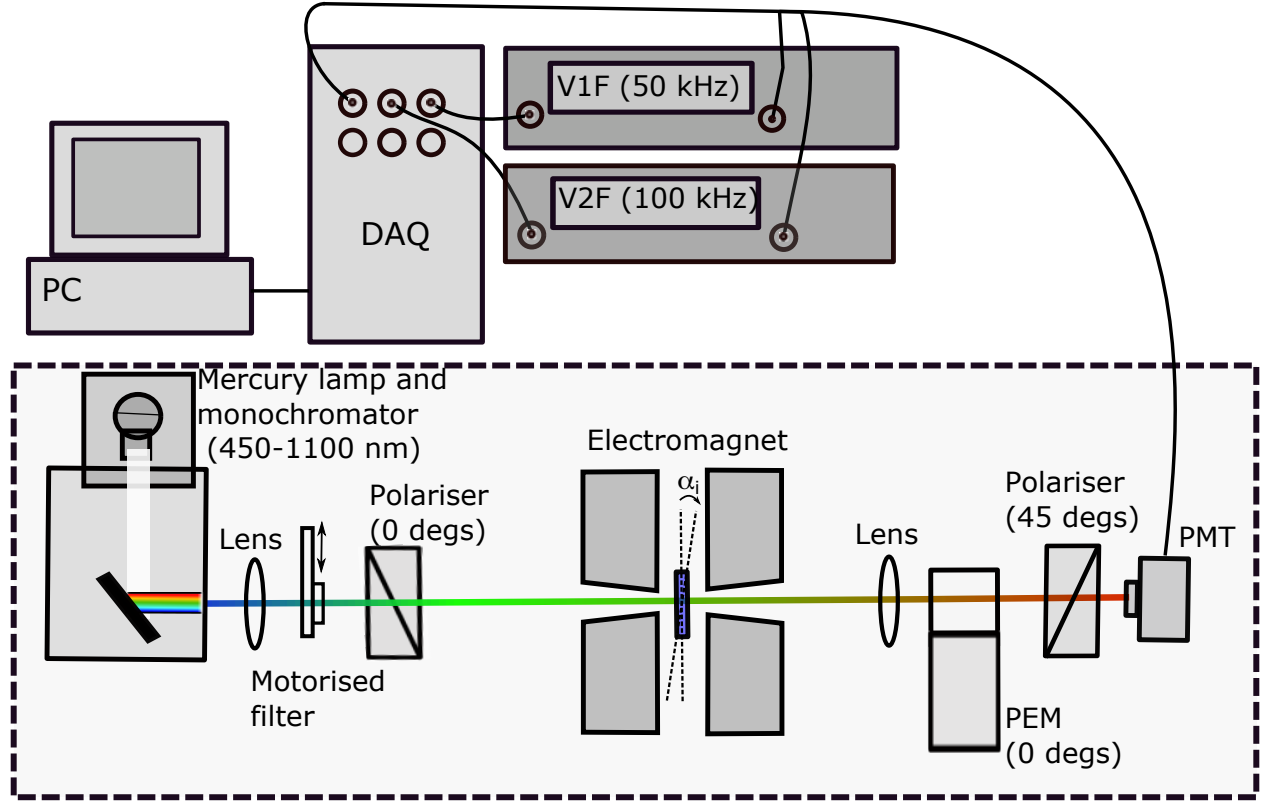


Figure 1: Schematic of the experimental configuration for the measurement of the spectral dependence of the Faraday effect.

The spectral dependence of the Faraday rotation and ellipticity is measured using a photoelastic modulator (PEM), as outlined in the schematic shown in Figure 1. These devices provide a fast, low-noise, and highly sensitive method to characterise the resulting light polarisation state after being transmitted through the sample. A mercury lamp is used as a broadband light source. Wavelengths are selected using a Newport Cornerstone monochromator. The monochromated light passes through a pair of lenses, and a polariser. Focusing lenses are used to maximize the light intensity passing through the narrow bore in the electromagnet and are placed before the first polariser, to ensure the incident polarisation state is linear *p*-polarisation. Additionally, a 400 nm high-pass filter cuts in for wavelengths longer than 600 nm to remove shorter harmonic wavelengths which arise from the monochromator grating. Light which is transmitted through the sample (at an incidence angle, α_i) passes out

through the second electromagnet pole piece and is collect by an addition focusing lens. This light then passes through the PEM and then the analysing polariser (which is set at 45 deg) before being focused onto the photomultiplier tube (PMT) (Hamamatsu H11901-20). The PEM and analysing polariser combination induces an oscillating signal with harmonics at 50 KHz and 100 KHz, which correspond to the first and the second harmonics of the PEM oscillation frequency. The first and second harmonic voltages from the PMT, referred to as V_{1F} and V_{2F} respectively, are measured with two Stanford Research Systems SR830 lock-in amplifiers, with analogue outputs feeding into a National Instruments data acquisition card. The DC PMT voltage (V_{DC}) is recorded directly by the data acquisition card. It has been shown elsewhere^{1,2} that the ratio of V_{1F}/V_{DC} and V_{2F}/V_{DC} are to a second-order approximation, directly proportional to the Faraday ellipticity (η_F) and Faraday rotation (θ_F) respectively. Using the Mueller-Stokes formalism, the following expression can be derived

$$\eta_F = \frac{1}{2\sqrt{2}J_1(A)} \frac{V_{1F}}{V_{DC}} \quad (1)$$

$$\theta_F = \frac{1}{2\sqrt{2}J_2(A)} \frac{V_{2F}}{V_{DC}} \quad (2)$$

where J_1 and J_2 are the first and second order Bessel functions of the first kind, respectively, with $A = 2.405$ rad.

Ellipsometry of a $\text{Tb}_{18}\text{Co}_{82}$ film

The experimentally derived diagonal (ε_{xx}) and off-diagonal (ε_{xy}) components of the permittivity tensor for a 30 nm $\text{Tb}_{18}\text{Co}_{82}$ film are shown in Figure 2 and Figure 3. The film is considered optically thick, such that any contribution from the substrate can be suitably neglected. The complex diagonal components, ε_{xx} were measured using standard ellipsometry with a PEM, as described in ref.³. With these values, the off-diagonal components, ε_{xy} can be extracted from measurements of the polar Kerr rotation and ellipticity. For this, the configuration outlined in Figure 1 is modified, such that the lens-PEM-polariser-PMT com-

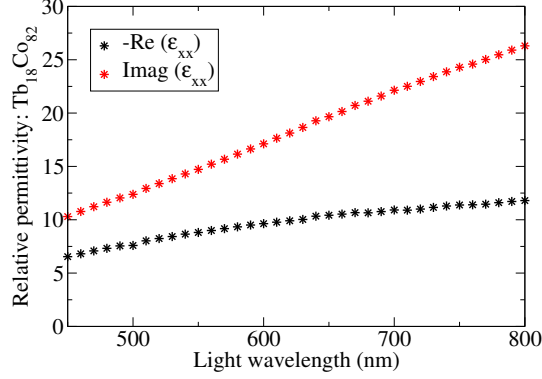


Figure 2: Experimental measurements of the real (black stars) and imaginary (red stars) part of the diagonal dielectric function elements ϵ_{xx} for $\text{Tb}_{18}\text{Co}_{82}$.

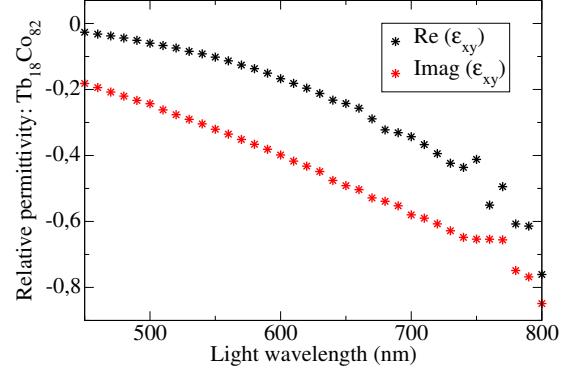


Figure 3: Experimental measurements of the real (black stars) and imaginary (red stars) part of the non-diagonal dielectric function elements ϵ_{xy} for $\text{Tb}_{18}\text{Co}_{82}$.

bination is moved to the left-hand side, such as to work in reflection, with a small incidence angle of 5 deg. This is the polar magneto-optical Kerr effect configuration and Equations (1) and (2) are still valid, but for the Kerr ellipticity and Kerr rotation respectively.

With measurements of the Kerr rotation (θ_K), Kerr ellipticity (η_K), as well as the diagonal permittivity ϵ_{xx} , the off-diagonal permittivity component ϵ_{xy} can be extracted using⁴:

$$\epsilon_{xy} = -i(\theta_K + i\eta_K) [\sqrt{\epsilon_{xx}}(\epsilon_{xx} - 1)] \quad (3)$$

Dimensionality and the plasmonic enhancement of the Faraday effect.

The spectral behaviour of the Faraday rotation (θ_F) and Faraday ellipticity (η_F) is shown in Figure 4. The plasmonic enhancement of the Faraday effect can be observed between 650 and 750 nm, for various truncated nanocone (TNC) base diameters. These measurements were performed at normal incidence with the light polarisation parallel to the 425 nm periodicity direction. As expected, with increasing base diameter, the Faraday enhancement red-shifts to longer wavelengths and becomes broader for both θ_F and η_F . This is consistent with the spectral broadening and red-shift associated with the weaker confinement of the LSP,

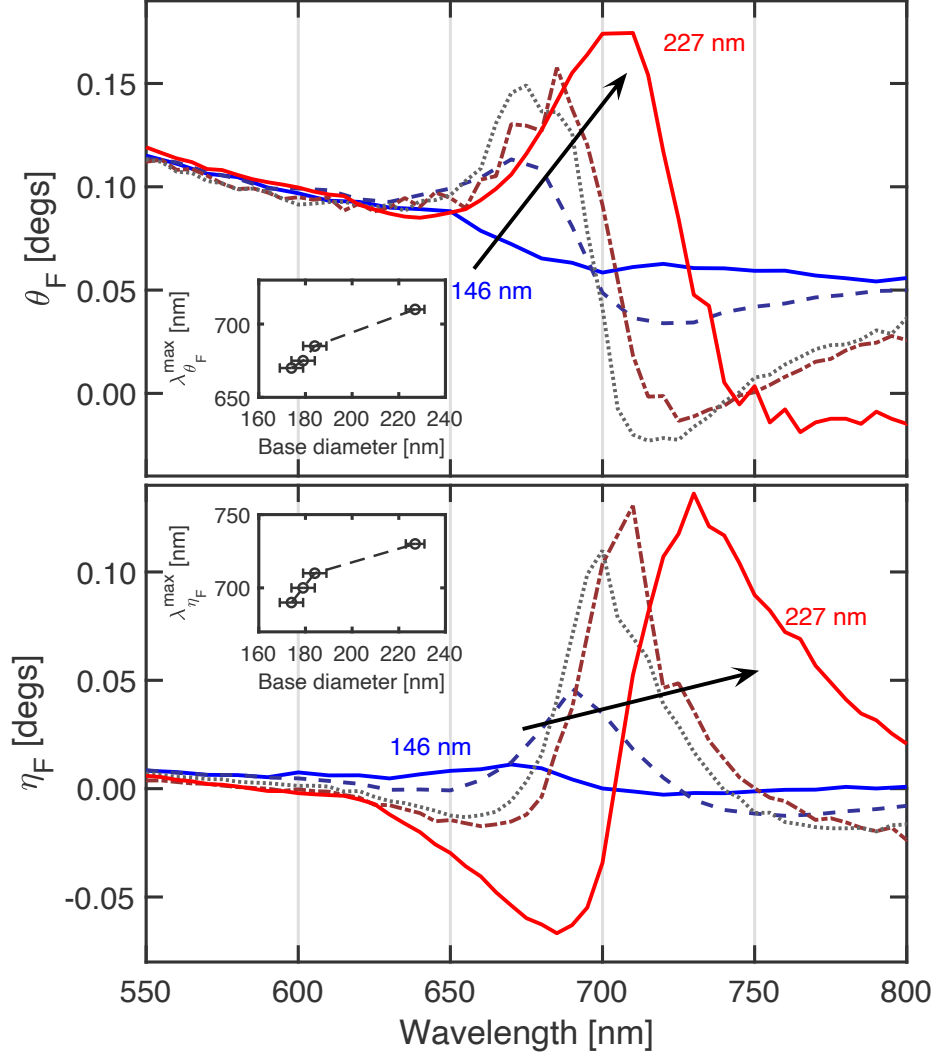


Figure 4: Comparison of the Faraday rotation (θ_F) and Faraday ellipticity (η_F) for different base diameter TNC arrays. The insets show the dependence of the peak θ_F and η_F wavelength as function of base diameter.

by reducing the depolarising field through retardation effects with increasing dimension⁵.

The wavelength for which the largest absolute value of θ_F and η_F occurs ($\lambda_{\theta_F}^{\max}$ and $\lambda_{\eta_F}^{\max}$ respectively) is plotted in the respective figure insets, against nanoantenna base-diameter.

Comparable trends are observed for both θ_F and η_F .

The enhancement of the Faraday effect is smaller for TNCs with reduced base diameter, since as the base diameter is reduced, the volume of the $\text{Tb}_{18}\text{Co}_{82}$ tip is reduced dramatically. Consequently, the magnetization falls off rapidly, and for base diameters below 146 nm, it is

not possible to measure the Faraday effect. Corresponding transmission curves for the three largest base-diameter TNCs are shown in Figure 5. The light polarisation is parallel to the 425 nm periodicity direction and a spectral broadening and redshift is observed for increasing base diameter. The wavelength of minimum transmission (λ_T^{\min}) is plotted alongside TNC base diameter, closely resembling the trend observed for $\lambda_{\theta_F}^{\max}$ and $\lambda_{\eta_F}^{\max}$ in Figure 4. There is a minimum observed at 425 nm associated with the Rayleigh anomaly of the air interface, the spectral position of which is independent of the TNC base diameter. Small peaks are observable at the onset of the LSP, at 616 nm. These are also independent of the TNC base diameter, and are a result of the Rayleigh anomaly at the fused-silica interface. There is no distinctive Fano-like lineshape due to the limited spectral overlap with the LSP when operating at normal incidence.

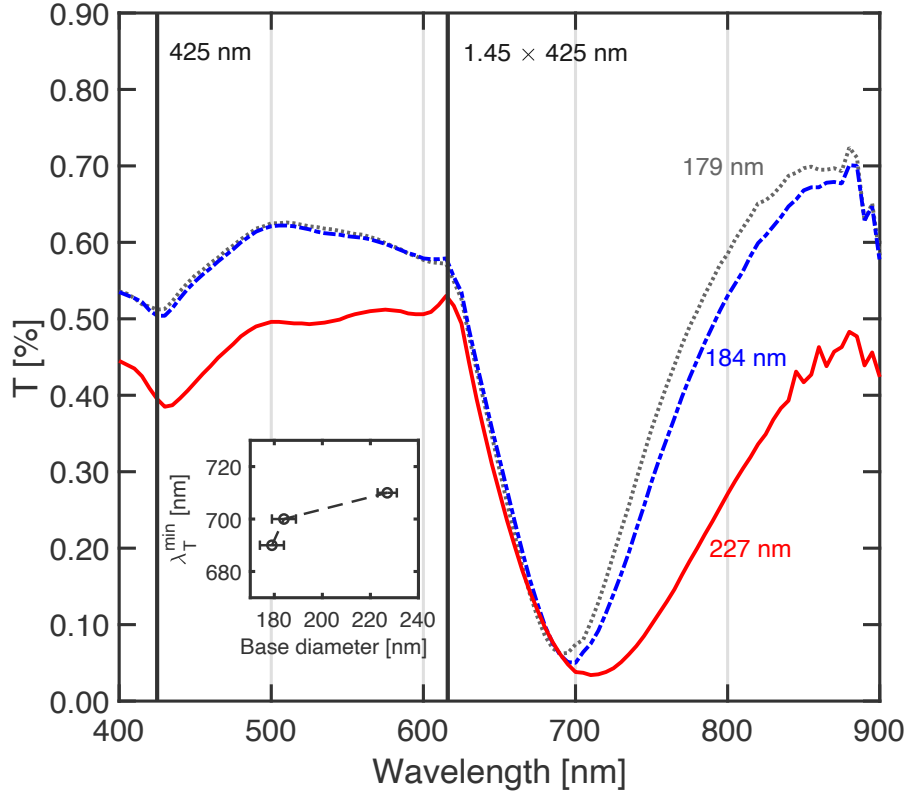


Figure 5: Comparison of the transmission spectra at normal incidence for different base diameter TNC arrays. The insets show the dependence of the wavelength of minimum transmission as function of base diameter.

Finite-element simulations

We use the COMSOL[®] Multiphysics 5.4 software to evaluate the magneto-optical properties of the magneto-plasmonic nanostructures considered in the paper. COMSOL[®] uses finite element methods to solve the following Maxwell equation:

$$\nabla \times \frac{\nabla \times \mathbf{E}(\mathbf{r})}{\mu_r} - \frac{\omega^2 \varepsilon(\omega)}{c^2} \mathbf{E}(\mathbf{r}) = 0, \quad (4)$$

where $\varepsilon(\omega)$ is the dielectric function of the material. In the case of magnetic materials the dielectric function is a 3×3 tensor. Assuming that the magnetization is along the z direction, the dielectric function reads:

$$\varepsilon(\omega) = \begin{pmatrix} \varepsilon_{xx}(\omega) & -\varepsilon_{xy}(\omega) & 0 \\ \varepsilon_{xy}(\omega) & \varepsilon_{xx}(\omega) & 0 \\ 0 & 0 & \varepsilon_{xx}(\omega) \end{pmatrix}, \quad (5)$$

where the off diagonal components are responsible for the magnetic circular dichroism (MCD). Values of the diagonal and off-diagonal components of the permittivity tensor used in these simulations were measured from a suitably thick Tb₁₈Co₈₂ film, as described in the Ellipsometry section of the Supporting Information.

In Equation 4, a harmonic time dependence has been assumed for the electric field: $\mathbf{E}(\mathbf{r}, t) = \mathbf{E}(\mathbf{r}) \exp(i\omega t)$. Since we are working in the optical regime, it is a good approximation for metals to neglect the response of the electrons to external magnetic fields, i.e. $\mu = \mu_0$. The magnetic induction is therefore obtained from the Faraday equation: $\mathbf{B}(\mathbf{r}) = -\nabla \times \mathbf{E}(\mathbf{r}) / (i\omega)$.

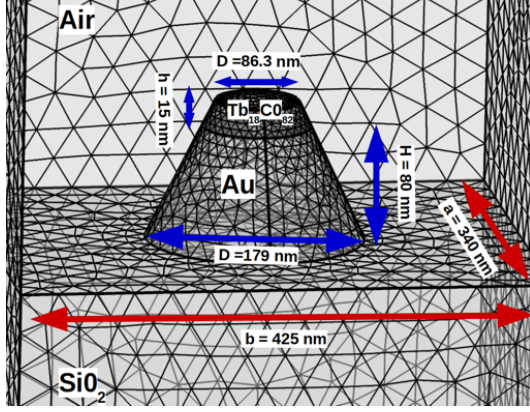


Figure 6: The magneto-plasmonic TNC structure modeled in COMSOL®.

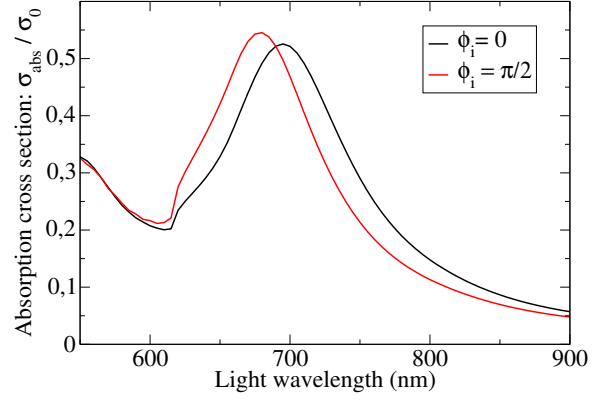


Figure 7: Normalised absorption spectrum calculated with COMSOL® for the TNC lattice based on the structure pictured in Figure 6. The incident light propagates in the z direction ($\alpha_i = 0$) with the electric field either along x ($\phi_i = 0$) or along y ($\phi_i = \pi/2$).

Transmission spectra simulations

The magneto-plasmonic nanostructure simulated in COMSOL® is depicted in the Figure 6, which consists of a truncated $\text{Tb}_{18}\text{Co}_{82}$ cone on top of a truncated gold cone. These are periodically arranged on a glass substrate with a refractive index $n_{\text{sub}} = 1.45$. Following the experimental data, the periodical lattice is rectangular with dimensions: $b = 425 \text{ nm} \times a = 340 \text{ nm}$. The Au layer is 80 nm thick with a base diameter of 179 nm and a truncation diameter of 101 nm. The magnetic $\text{Tb}_{18}\text{Co}_{82}$ layer is 15 nm thick with a truncation diameter of 86.3 nm. We have implemented the frequency dependent dielectric functions for $\text{Tb}_{18}\text{Co}_{82}$ obtained from experimental measurements, (see Figures 2-3). For gold we took the values given by Johnson and Christy⁶.

In the simulation, the magneto-plasmonic TNC is interacting with p-polarised light. Floquet periodic boundary conditions are used to simulate the lattice periodicity. We consider two different configurations. In the first configuration, the incident light propagates in the $x - z$ plane ($\phi_i = 0 \text{ deg}$) with an incident angle α_i with respect to the z axis. In the second configuration, the incident light propagates in the $y - z$ plane ($\phi_i = 90 \text{ deg}$) with an incident angle α_i with respect to the z axis. Here, the directions x and y denote, respectively, the

small and large lattice directions. The incident electric field (E_{inc}) is described by:

$$\mathbf{E}_{\text{inc}} = E_0 \begin{pmatrix} \cos \alpha_i \cos \phi_i \\ \cos \alpha_i \sin \phi_i \\ \sin \alpha_i \end{pmatrix} \exp [i (-k_0 (x \sin \alpha_i \cos \phi_i + y \sin \alpha_i \sin \phi_i - z \cos \alpha_i) + \omega t)], \quad (6)$$

where $k_0 = 2\pi n_{\text{air}}/\lambda$ corresponds to the light wave-vector in the air ($n_{\text{air}} = 1$). In Fig. 7, we plot the absorption cross section of the magneto-plasmonic lattice structure calculated with COMSOL[®] using linearly polarised light at normal incidence ($\alpha_i = 0$). The maximum of absorption corresponds to the excitation of localized surface plasmon (LSP) in the truncated gold structure. We observe that the excitation of the LSP along the 340 nm lattice direction is red-shifted compare to the 435 nm lattice direction. This is caused by dipole-dipole interactions^{7,8} that are different for the $\phi_i = 0$ deg and the $\phi_i = 90$ deg configurations.

Due to the nanometric structure of the lattice, the light can be diffracted in different directions. The number of diffracted directions or modes leading to constructive interference is very large, and the different modes are labeled by two integers n and m . Most of the modes stay close to the surface of the lattice with only few of them excited at the substrate. As discussed in the main text, the criteria for these modes is that the component of the light wave-vector normal to the lattice surface is real:

$$k_{\perp} = \sqrt{k_s^2 - (\mathbf{k}_{\parallel} + m\mathbf{G}_1 + n\mathbf{G}_2)^2} > 0. \quad (7)$$

In the above formula, $k_s = 2\pi n_{\text{sub}}/\lambda$ corresponds to the light wave-vector in the substrate, $\mathbf{k}_{\parallel} = k_0 [\sin(\alpha_i) \cos(\phi_i) \mathbf{u}_x + \sin(\alpha_i) \sin(\phi_i) \mathbf{u}_y]$ corresponds to the wave-vector component parallel to the lattice surface and $\mathbf{G}_1 = 2\pi/a \mathbf{u}_x$, $\mathbf{G}_2 = 2\pi/b \mathbf{u}_y$ are the reciprocal lattice vectors.

In Figure 8, we plot the number of diffracted modes that fulfill Equation (7) as a function of the light wavelength and the angle of incidence α_i . We notice that only a few number of

diffraction modes $(m ; n)$ are propagating, especially for large wavelengths where only one mode $(m = 0 ; n = 0)$ is allowed. The latter corresponds to the normal refracted light mode given by the Snell-Descartes law. As expected, the number of diffracted modes increases when the light wavelength decreases. Moreover, the number of diffracted modes strongly depends on the propagation direction of the incoming light. In the case of an electric field with a parallel component along the 340 nm lattice direction $(\phi_i = 0)$, there is almost no dependence in the incident angle α_i for frequencies above 700 nm. On the contrary, for the 425 nm direction $(\phi_i = 90 \text{ deg})$, the number of diffracted modes is changing between 1 and 2 above 700 nm with a separation line that is almost linear with the incident angle α_i . This behaviour can also be observed in the $\phi_i = 0$ configuration, but for shorter wavelengths. The separation line corresponds to the addition of the diffracted mode $(n = 0 ; m = -1)$ for $\phi_i = 0 \text{ deg}$ and $(n = -1 ; m = 0)$ for $\phi_i = 90 \text{ deg}$ and can be obtained analytically from Equation (7):

$$\lambda_{\text{R}}^{[0,-1]} = a [n_{\text{sub}} + n_{\text{air}} \sin(\alpha_i)] \quad \text{for } \phi_i = 0^\circ, \quad \lambda_{\text{R}}^{[-1,0]} = b [n_{\text{sub}} + n_{\text{air}} \sin(\alpha_i)] \quad \text{for } \phi_i = 90^\circ, \quad (8)$$

where the linear relation between λ and α_i is recovered for small angles.

The experimental transmission spectra presented in Figure 1 of the main text shows a strong anisotropic angular dependence, which we were able to reproduce and to understand from the COMSOL[®] simulations.

Comparing Figure 7 and the transmission spectra in Figure 1 of the main text, we observe that the minimum of transmission occurs at the maximum of the absorption spectrum, precisely where the LSP modes are strongly excited. However, it is also clear that the maximal attenuation of the transmission occurs when there are no diffracted modes, other than the mode $(n = 0 ; m = 0)$.

This type of behavior has been discussed in several papers^{7,9,10} and originates from a

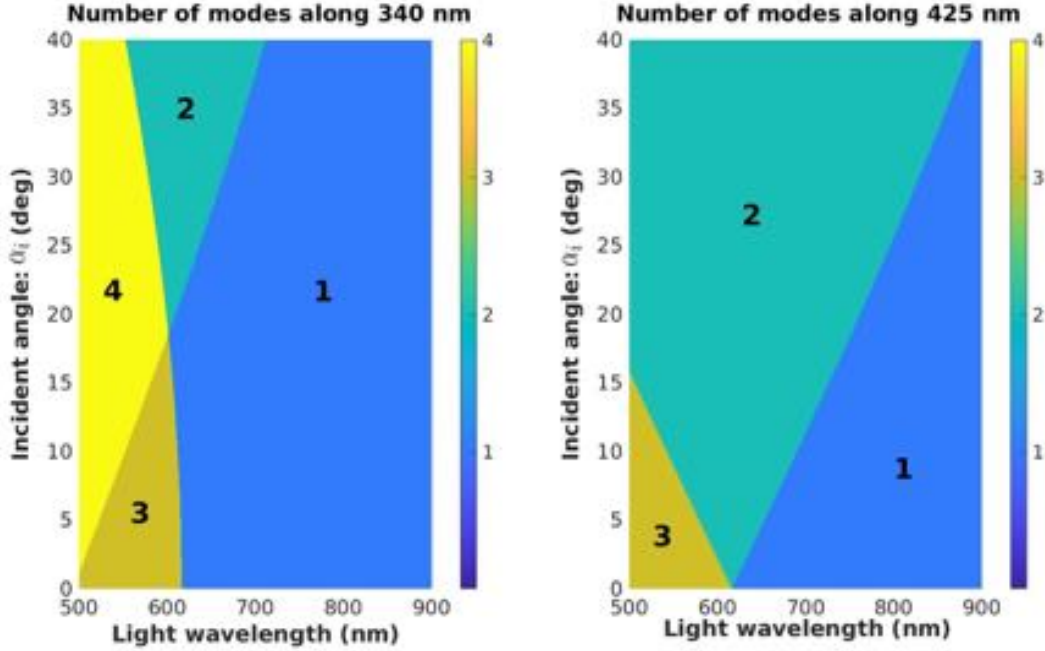


Figure 8: Number of diffracted modes propagating across the substrate as a function of the incident angle α_i and light wavelength for a rectangular lattice ($340 \text{ nm} \times 425 \text{ nm}$). Two different configurations are shown. In the left panel k_{\parallel} is along the short lattice direction $a = 340 \text{ nm}$, whereas in the right panel k_{\parallel} is along the long lattice direction $b = 425 \text{ nm}$.

Fano coupling between LSP and surface lattice diffraction modes. A complete discussion can be found in the review paper by Kravets et al.⁸. When one of the diffracted modes travel exactly along the lattice surface at a frequency close to the LSP resonance, then the latter interacts with many plasmonic nanostructures, thus enhancing the energy transfer from the light to the LSP. However, if the diffracted mode does not stay close to the lattice surface but instead activates through the substrate, then it is no longer contributing to LSP excitation. As a consequence, we expect a relative reduction in the extinction cross section and an increase of the transmission.

This explains why the transmission curves for $\phi_i = 0 \text{ deg}$ are almost independent of α_i , because in this particular configuration there is no overlap between the LSP mode and the lattice diffraction modes. On the contrary, for $\phi_i = 90 \text{ deg}$, there is an overlap between the LSP mode and a lattice diffraction mode which causes the red-shift and the increase in amplitude of the transmission spectra.

Near field calculations around the TNC

It is well known that a dipole can not radiate along the dipole axis. As such, the excitation of the $\lambda_R^{[-1,0]}$ for the $\phi = 90$ deg configuration would seem incompatible for p-polarised light since the in-plane component of the incident light field would induced a dipole oscillation parallel to the $\lambda_R^{[-1,0]}$ mode. The near field maps of the TNC (Figure 9) show that with oblique incidence light there exists and enhancement of the E-field around the tip of the TNC. This is indicative of an out-of-plane component to the induce electric dipole in the TNC. This out-of-plane component is capable of exciting all in-plane modes, e.g. $[-1,0]$, $[0,-1]$ and $[-1,-1]$ modes.

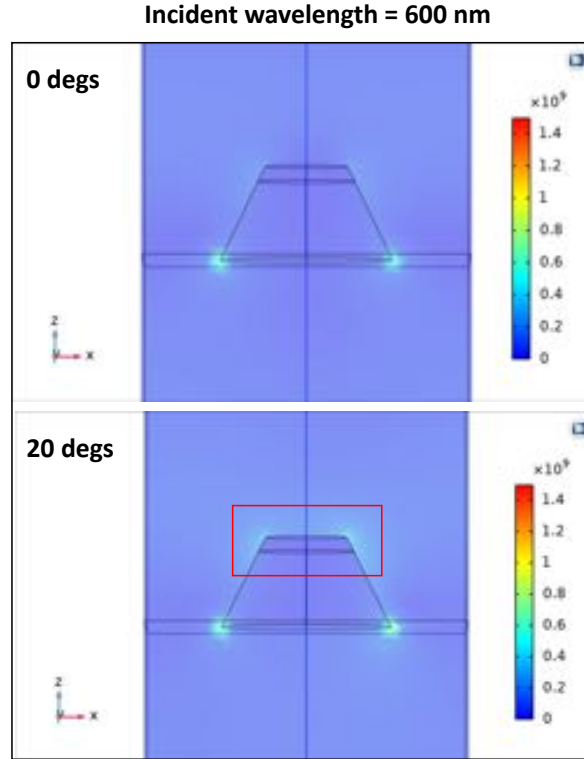


Figure 9: Near field maps of the E-field magnitude in the local vicinity of the TNC under illumination at incidence angles $\alpha_i = 0$ and 90 degs (top and bottom rows, respectively) for a 600 nm wavelengths. The red rectangle emphasises the field enhancement at the tip associated with the oblique incidence of the incident E-field.

Faraday spectra simulations

Enhancement and tunability of magneto-optical Faraday effects have been observed in our experimental data. In our COMSOL[®] simulations, magneto-optical effects are examined by computing the ratio between the small and the large component of the electric field. The latter are obtained from the following formulas:

$$\Theta_F = \frac{\int_{\Omega} \arctan(-E_y/E_x) dV}{\int_{\Omega} dV} \text{ for } \phi_i = 0, \quad \Theta_F = \frac{\int_{\Omega} \arctan(E_x/E_y) dV}{\int_{\Omega} dV} \text{ for } \phi_i = 90^\circ, \quad (9)$$

where the integral is performed over a finite volume in the substrate located between $2.5 \mu\text{m}$ and $3 \mu\text{m}$ far away from the magneto-plasmonic structures. The magneto optical Faraday effect $\Theta_F = \theta_F + i\eta_F$ can be decomposed into two different effects: The Faraday rotation $\theta_F = \Re(\Theta_F)$ and the Faraday ellipticity $\eta_F = \Im(\Theta_F)$ which correspond, respectively, to a rotation of the polarisation plane and to a measure of the light ellipticity. Faraday effects originate from differences in the propagation between circular right and circular left polarised light. Such differences appear when light interacts with chiral structures or with magnetic materials.

In the experiments, the magnetization of $\text{Tb}_{18}\text{Co}_{82}$ is controlled by an external magnetic field and is either saturated in the $+z$ or $-z$ direction. In our COMSOL[®] simulations, magnetization reversal is included in the dielectric function of the material:

$$\varepsilon(\omega) = \begin{pmatrix} \varepsilon_{xx}(\omega) & -M_s \varepsilon_{xy}(\omega) & 0 \\ M_s \varepsilon_{xy}(\omega) & \varepsilon_{xx}(\omega) & 0 \\ 0 & 0 & \varepsilon_{xx}(\omega) \end{pmatrix}, \quad (10)$$

where $M_s = \{-1, 1, 0\}$ corresponds, respectively, to a magnetization in the $+z$ direction, in the $-z$ direction and to no magnetization.

We have encountered some convergence problems when calculating the magneto-optical Faraday effects in COMSOL[®]. In Figure 10, we plot the Faraday rotation in the following

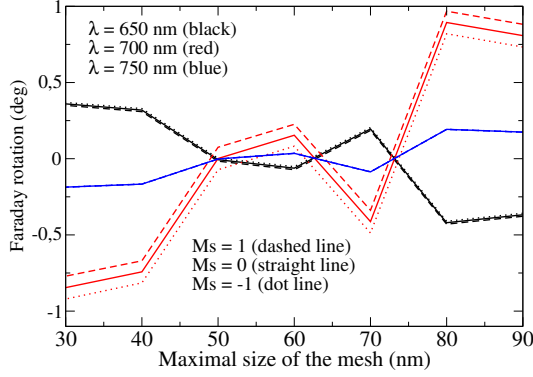


Figure 10: COMSOL® simulations: Faraday rotation as a function of the mesh size for different magnetic configurations $M_s = \{-1, 0, 1\}$ and different light wavelength $\lambda = \{650 \text{ nm}, 700 \text{ nm}, 750 \text{ nm}\}$. The incident light is along the 425 nm lattice direction ($\phi_i = 90 \text{ deg}$) and at normal incidence ($\alpha_i = 0 \text{ deg}$).

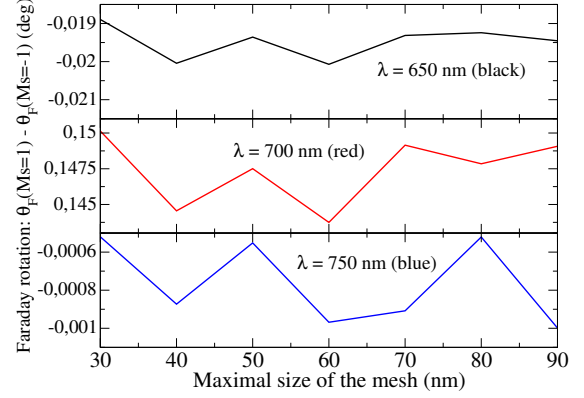


Figure 11: COMSOL® simulations: Difference between the Faraday rotation calculated in Fig. 10 with a magnetization in the $+z$ direction ($M_s = 1$) and in the $-z$ direction ($M_s = -1$) as a function of the mesh size.

configuration $\alpha_i = 0$ and $\phi_i = 0 \text{ deg}$ for different wavelengths and for different magnetization states of $\text{Tb}_{18}\text{Co}_{82}$ as a function of the mesh size. Surprisingly, we were not able to make the calculation converge by decreasing the size of the mesh. We expect that the Faraday rotation should go to zero for $M_s = 0$ for all wavelengths, because there should be no physical differences between circular right and circular left propagating light, but we instead observe no clear dependence on the mesh size. We could not clearly determine the origin of this behaviour, but we suspect that it is due to the fact that the meshing is not chiral even if the structure is. Nevertheless, we can still make use of this data, because we observe that the change in optical rotation upon magnetization reversal is in fact converged. In the Figure 11, we plot the difference between $M_s = +1$ and $M_s = -1$. We notice that the difference is converged up to 0.005 deg, which is more than sufficient accuracy for comparison with the experimental data, which is nearly two orders of magnitude larger. Therefore, to compute the magneto-optical Faraday effects, we take a maximal mesh size of 50 nm and we subtract the $M_s = -1$ from the $M_s = +1$ simulations to remove the mesh contribution.

References

- (1) Oakberg, D. T. C. Hinds Instruments: Application Note, Magneto-Optic Kerr Effect. 2010.
- (2) Sato, K. *Japanese Journal of Applied Physics* **1981**, *20*, 2403–2409.
- (3) Jellison, G. E.; Modine, F. A. In *Handbook of Ellipsometry*; Tompkins, H. G., Irene, E. A., Eds.; William Andrew Publishing: Norwich, NY, 2005; pp 433–480.
- (4) Zvezdin, A. K.; Kotov, V. A, *Modern Magnetooptics and Magneto-optical Materials*; CRC Press, 1997.
- (5) Maier, S. A.; Atwater, H. A. *Journal of Applied Physics* **2005**, *98*, 011101.
- (6) Johnson, P. B.; Christy, R. W. *Phys. Rev. B* **1972**, *6*, 4370–4379.
- (7) Haynes, C.; McFarland, A.; Zhao, L.; Van Duyne, R.; Schatz, G.; Gunnarsson, L.; Prikulis, J.; Kasemo, B.; Käll, M. *Journal of Physical Chemistry B* **2003**, *107*, 7337–7342.
- (8) Kravets, V. G.; Kabashin, A. V.; Barnes, W. L.; Grigorenko, A. N. *Chemical Reviews* **2018**, *118*, 5912–5951, PMID: 29863344.
- (9) Kravets, V. G.; Schedin, F.; Grigorenko, A. N. *Phys. Rev. Lett.* **2008**, *101*, 087403.
- (10) Liu, F.; Zhang, X. *68*, 719–725.

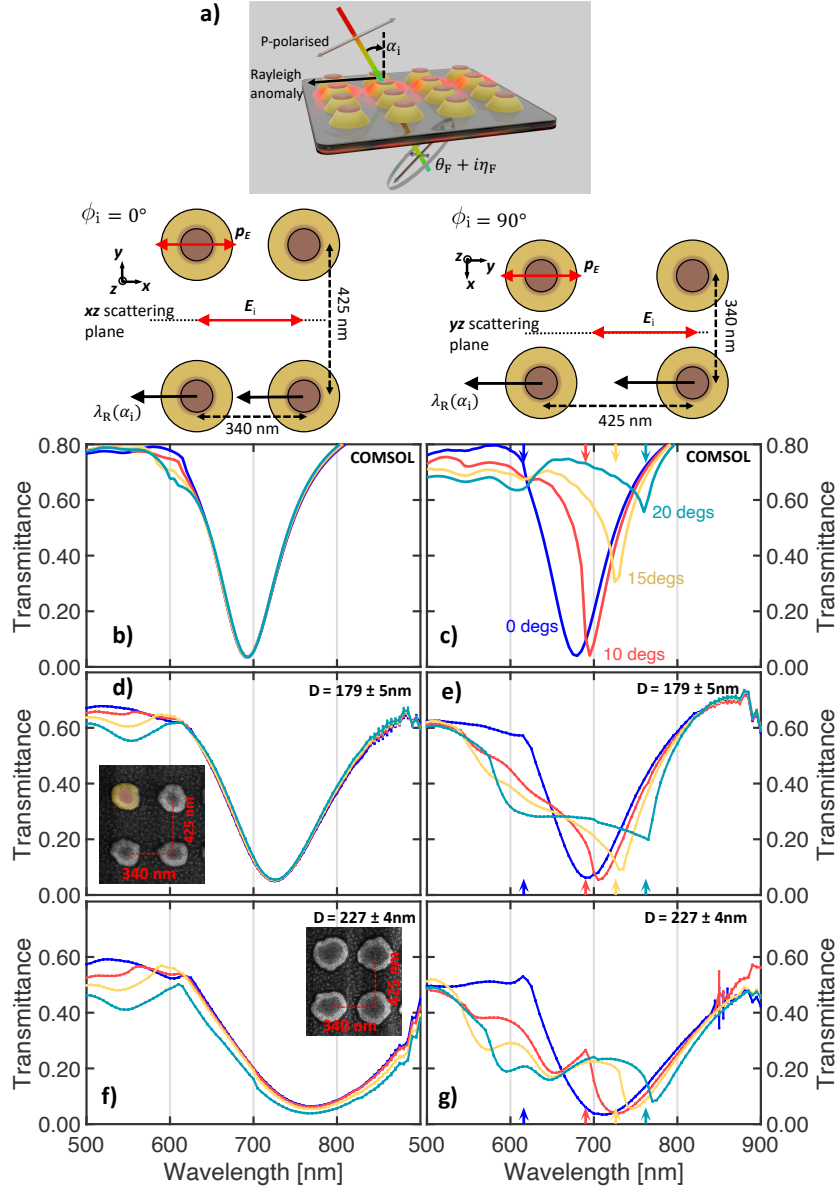


Figure 1: a) Schematic representation of the TNC array and resulting Faraday rotation (θ_F) and ellipticity (η_F) of the transmitted light. The Rayleigh anomaly, excited at $\lambda_R^{[n,m]}(\alpha_i)$, is depicted by the laterally excited beam associated with the *passing-off* of the diffraction order. Below are schematic representations of the TNC lattice for the two azimuthal orientations ($\phi_i = 0$ and 90°) with respect to the incident light polarisation (E_i) and scattering plane, with p_E denoting the orientation of the electric dipolar plasmon in the individual TNCs. b), c) Calculated transmission spectra for incidence angles from 0 - 20 degrees, with the scattering plane orientated along the 340 nm periodicity (left column) and the 425 nm periodicity (right column). d), e) Measured transmission spectra for the $D_B = 179 \text{ nm}$ TNC array, with a scanning electron microscopy figure inset of the TNC array. f), g) Same as d), e) but for the $D_B = 227 \text{ nm}$ TNC array.

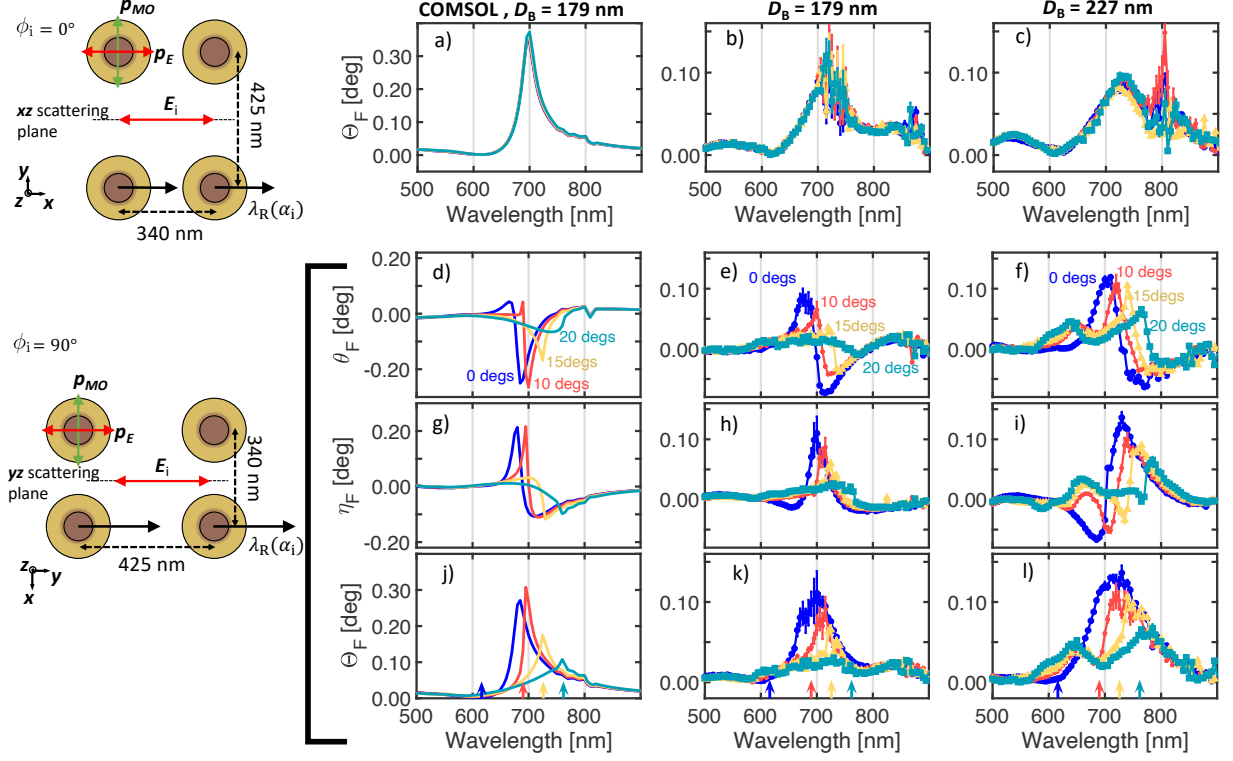


Figure 2: Spectral dependence of Faraday effect as calculated in COMSOL[®] for a $D_B = 179$ nm TNC array (left column), as measured for the $D_B = 179$ nm TNC array (middle column) and as measured for the for a $D_B = 227$ nm TNC array. a) – c) Θ_F for the $\phi_i = 0$ configuration. d) – l) Spectral dependence of θ_F (d) – f)), η_F (g) – i)) and Θ_F (j) – l)), for the $\phi_i = 90$ configuration. A quadratic polynomial has been fitted to the θ_F measurements and subtracted to remove the background contribution which arises from the Faraday rotation of the fused-silica substrate, which is strongest for short wavelengths and approaches zero with increasing wavelength. Schematics on the left hand side depict the TNC array orientation with respect to the scattering plane and incident polarisation (E_i) for the $\phi_i = 0$ and 90 configurations. The orientation of the electric dipolar plasmon is depicted by p_E and the spin-orbit induced magneto-optical dipolar plasmon orientation is depicted by p_{MO} .

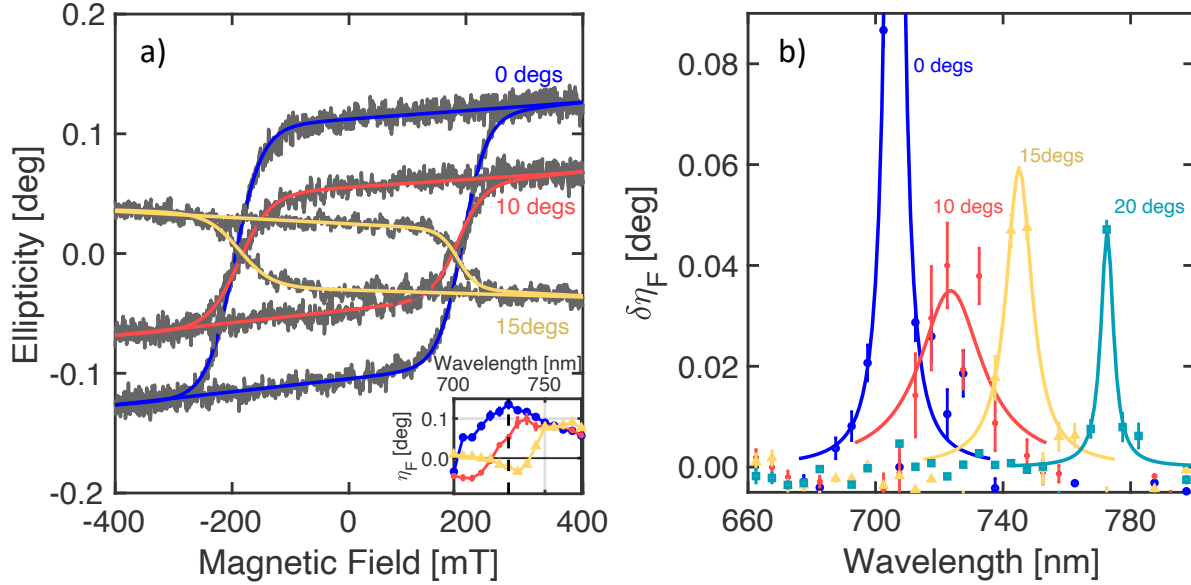


Figure 3: a) Hysteresis loops recorded at a wavelength of 730 nm demonstrating how the magnitude and sign of the Faraday ellipticity (η_F) can be controlled through the incidence angle (α_i). The inset shows a magnified view of the η_F for $\alpha_i = 0$ (blue circles), 10 (red diamonds), and 15 degrees (yellow triangles). The dashed vertical line indicates the 730 nm wavelength where the hysteresis loops in the main figure were recorded. b) The change in Faraday ellipticity ($\delta\eta_F$) between successive wavelengths. Following the onset of the SLM, there is an abrupt change in light ellipticity which is associated with a maximum in $\delta\eta_F$. The peaks have been fitted with Lorentzian peak functions.

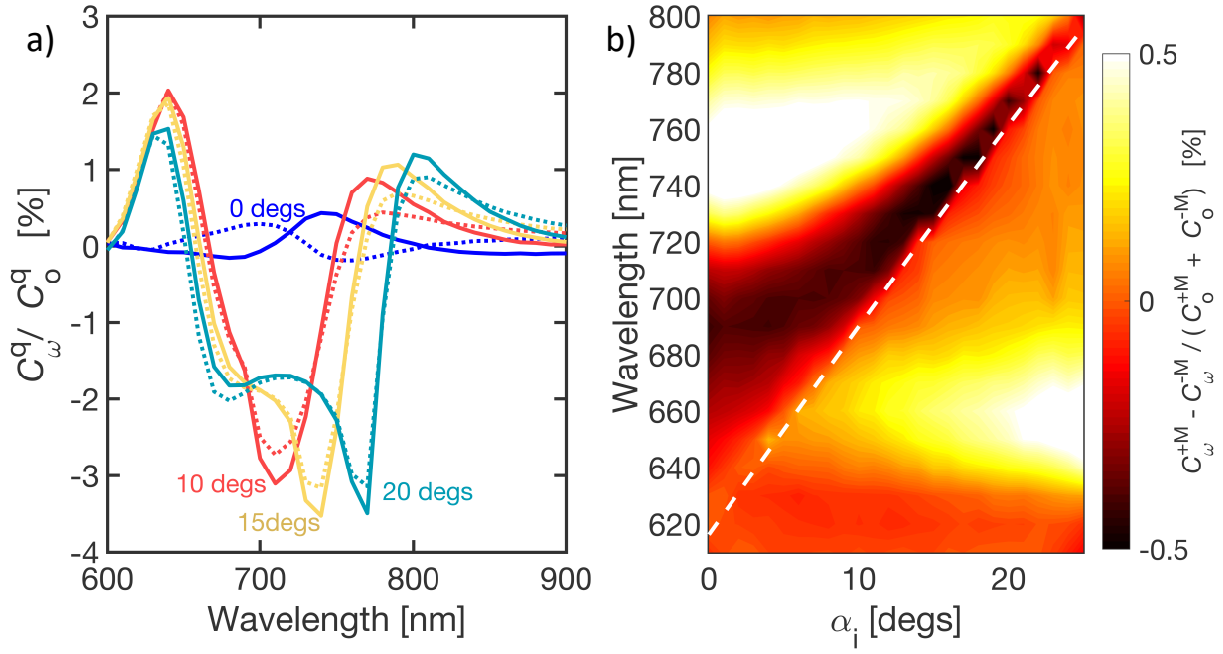


Figure 4: a) Spectral dependence of the C_ω^q/C_o^q signals, where $q = +M$ or $-M$ for the solid and dashed curves respectively. C_ω^q is related to the total circular dichroism for a particular magnetization state, containing both magnetic and non-magnetic contributions. b) The amplitude of the magnetic modulation of the helicity dependent transmission as function of both wavelength and α_i , which relates to the difference between the solid and dashed curves in Figure 4 a). The dashed white line indicates the expected location of the Rayleigh anomaly calculated from Eq. (3).